

An Automated End-to-End Deep Learning-Based Framework for Lung Cancer Diagnosis by Detecting and Classifying the Lung Nodules

Samiul Based Shuvo^{a,*}, Tasnia Binte Mamun^a

^aDepartment of Biomedical Engineering, Bangladesh University of Engineering and Technology, Dhaka-1205, Bangladesh,

ARTICLE INFO

Keywords:
Deep Learning
Lung Segmentation
Lung Nodule
Lung Cancer
U-Net
Vision Transformer
YOLO-V5

ABSTRACT

Objective: Lung cancer is one of the leading causes of cancer-related deaths worldwide, and early detection is crucial to improve patient outcomes. However, early diagnosis is a major challenge, particularly in low-resource settings with limited access to medical resources and trained radiologists. This study aims to propose an automated end-to-end deep learning-based framework for the early detection and classification of lung nodules, specifically for low-resource settings. **Methods:** The proposed framework consists of three stages: lung segmentation using a modified 3D U-Net, named 3D Res-U-Net, nodule detection using YOLO-v5, and classification with a Vision Transformer-based architecture. We evaluated the proposed framework on the publicly available dataset, LUNA16. The performance of the proposed framework was measured using the respective domain's evaluation metrics. **Results:** The proposed framework achieved a 98.82% lung segmentation dice score while detecting the lung nodule with 0.76 mAP@50 from the segmented lung at a low false positive rate. The performance of both networks in the proposed framework was compared with other studies, and they were found to outperform them in terms of segmentation and detection accuracy. Furthermore, our proposed Vision transformer network achieved an accuracy of 93.57%, which is 1.21% higher than the state-of-the-art networks. **Conclusion:** Our proposed end-to-end deep learning-based framework can effectively segment the lung and detect and classify lung nodules, particularly in low-resource settings with limited access to radiologists. The proposed framework outperforms existing studies across all respective evaluation metrics. **Significance:** The proposed framework can potentially improve the accuracy and efficiency of lung cancer screening in low-resource settings, ultimately leading to better patient outcomes. Our study demonstrates that deep learning-based approaches can be applied effectively to automated lung cancer detection and classification, even in settings with limited medical resources and trained personnel.

1. Introduction

Lung cancer has the most significant mortality rate (18.7%) and the second-highest incidence rate (12.4%) among all malignant tumours worldwide, according to statistics from the GLOBOCAN 2022 cancer report [1]. Almost half (49%) of all lung cancer cases now occur in countries ranked as medium to low on the Human Development Index (HDI) [2]. Just 15% of lung cancer patients survive five years after diagnosis, and 70% have either locally progressed or distant metastases[3]. The primary cause of this is that individuals with early-stage lung cancer frequently do not show any symptoms, leading to a delayed diagnosis and worse outcomes. Pulmonary nodules are the main symptom of early-stage lung cancer, and early identification of lung cancer is essential for increasing survival rates[4, 5]. Accurately identifying lung nodules with a diameter between 3mm and 30mm is essential for early diagnosis and lowering mortality rates. Doctors use computed tomography (CT) imaging to detect pulmonary nodules and identify early-stage lung cancer. However, in developing nations, access to this technology is limited due to insufficient medical equipment and supplies. Additionally, CT exams are time-consuming and challenging, requiring radiologists to examine hundreds of images. This increases the likelihood of misdiagnosis.

The automatic diagnosis of pulmonary nodules presents several challenges, such as the significant disparity between the number of positive and negative samples, the varying shapes of nodules, and the lack of integrated approaches [5, 6]. Computer-aided diagnosis (CAD) can help address these issues by assisting doctors, speeding up diagnoses, and reducing the number of incorrect diagnoses.

This study presents a deep-learning model for automatically locating pulmonary nodules and determining whether they are malignant. The proposed model consists of three phases that identify and categorize pulmonary nodules. A 2D-based YOLOv5 network detects lung nodules on axial slices after the lung is segmented using a novel 3D Res-U-Net-based lung segmentation network. This process identifies the region of interest (ROI). The third and final phase is a 2D classification network that extracts nodule characteristics and forecasts their diagnostic score using a self-attention-based vision transformer. The patch of the slice is extracted according to the ROI predicted by the detection network. A flow diagram of the proposed proposed model is shown in Fig. 1.

The key contributions of this work are summarized as follows:

- We established the proposed model using multi-stage models. Our framework can reliably and accurately identify and categorize pulmonary nodules, reducing the burden on clinicians and the rate of incorrect diagnoses.

*Corresponding author

 sbshuvo@bme.buet.ac.bd (S.B. Shuvo); tasnia@bme.buet.ac.bd

(T.B. Mamun)

ORCID(s): 0000-0002-5035-2114 (S.B. Shuvo)

Table 1

Summary of Works Carried out in Segmentation, Nodule Detection and Classification Domain on Lung CT

| Lung Segmentation Task | | | |
|----------------------------|--|-----------------------|-------------------------------------|
| Author | Dataset | Network | Dice Score(%) |
| Kendall et al. [8] (2017) | LUNA16 | Segnet | 96.52 |
| Alom et al. [9] (2019) | LUNA16 | R2U-Net | 98.80 |
| Khanna et al. [10] (2020) | LUNA16 | ResNet 34 based U-Net | 96.57 |
| Jalali et al. [11] (2021) | LIDC-IDRI | BCDU-Net | 97.31 |
| Francis et al. [12] (2022) | AAPM Lung CT Segmentation Challenge 2017 dataset | 3D U-Net | Left lung: 97.9 Right Lung: 97.3 |
| Lijing et al. [13] (2024) | LIDC-IDRI | U-Net | 88.17 |

| Lung Nodule Detection Task | | | |
|----------------------------|---------|-----------------|--------|
| Author | Dataset | Network | mAP@50 |
| Cai et al. [14] (2020) | LUNA16 | Mask R-CNN | 0.88 |
| Shao et al. [15] (2021) | LUNA16 | Yolo v5 refined | 0.75 |
| Zhou et al. [16] (2022) | LUNA16 | Yolo v5(s) | 0.75 |
| Liu et al. [17] (2022) | LUNA16 | STBi-YOLO | 0.95 |
| Liu et al. [18] (2025) | LUNA16 | Mask R-CNN | 0.97 |

| Lung Nodule Malignancy Classification Task | | | |
|--|-----------|-------------|-------------|
| Author | Dataset | Network | Accuracy(%) |
| Filho et al. [19] (2018) | LIDC-IDRI | CNN | 92.63 |
| Xie et al. [20] (2018) | LIDC-IDRI | DCNN | 89.53 |
| Huang et al. [21] (2022) | LIDC-IDRI | SSTL-DA | 91.07 |
| Wu et al. [22] (2023) | LIDC-IDRI | STLF-VA | 92.36 |
| Lijing et al. [13] (2024) | LIDC-IDRI | Nodule-CLIP | 90.6 |

- We proposed a novel 3D Res-U-Net algorithm, which can segment the lung with state-of-the-art performance.
- We utilized the YOLOv5 detection algorithm, which can detect lung nodules with high confidence and performance.
- We utilized a novel vision transformer-based classification network to classify cancerous nodules.
- Our proposed approach achieves an 89.5% dice score for lung segmentation, an 89% lung nodule detection mAP on the LUNA16 dataset [7], and 86.75% cancer classification accuracy.

The remainder of this paper is organized as follows. Section 2 reviews related work in the field of lung cancer detection and highlights the strengths and limitations of existing approaches. Section 3 presents utilized datasets and their preprocessing schemes. In Section 4, we introduce the design of the proposed model in detail, including three architectures employed and the evaluation metrics used to assess the framework’s performance. Section 6 presents the experimental results, and 7 discusses the strengths and limitations of our proposed approach. Finally, Section 8 summarizes the

contributions of this work and outlines directions for future research.

2. Related Works

As previously discussed, several studies have explored segmenting the lung parenchyma, identifying nodules, and categorizing malignant nodules using machine learning and deep learning-based frameworks, utilizing both publicly and privately available datasets. In this section, we provide an overview of research activities in this domain, as shown in Table 1).

3. Materials and methods

In this section, we provide an overview of the dataset used and the signal preprocessing stages.

3.1. Dataset

The Lung Nodule Analysis (LUNA16) Dataset, which is a subset of the LIDC-IDRI dataset[23], is used in this study. LIDC-IDRI contains 1018 low-dose CT scans and annotations from multiple radiologists. The case name, centroid coordinates of the nodule, diameter, volume of the nodule, texture of the nodule, and results of multiple radiologists are included in LIDC-IDRI. CT images of LIDC-IDRI with a

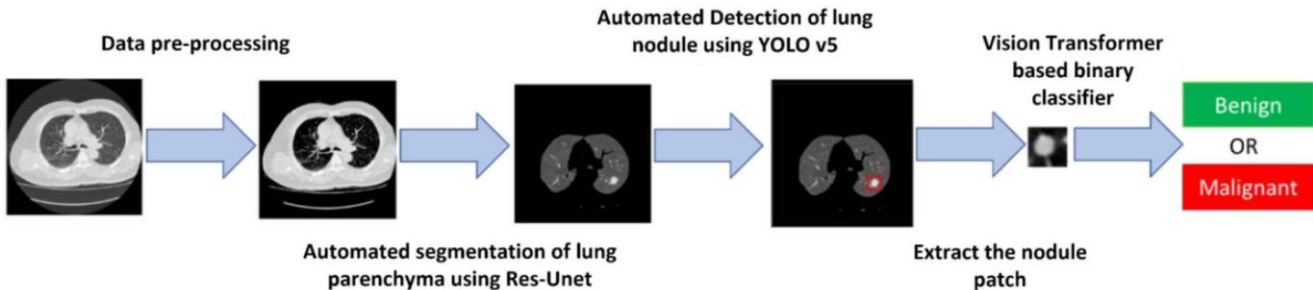


Figure 1: A graphical overview of the end-to-end deep learning-based framework for lung cancer detection workflow

slice thickness of more than 2.5 mm are eliminated from the LUNA16 dataset. This dataset was created to facilitate the development of automated nodule detection systems for clinical use as part of the 2016 International Symposium on Biomedical Imaging (ISBI) Lung Nodule Analysis (LUNA) Challenge. It consists of CT scans from 888 patients, with 1,186 nodules annotated by four experienced radiologists. To ensure accuracy, a two-phase annotation process was used, and nodules larger than 3mm were considered by all four radiologists [7]. Therefore, nodules smaller than 3 mm or with only one or two radiologists' annotations are excluded. Thus, 888 low-dose CT scans are produced. It also includes a lung segmentation binary mask for each CT scan. This dataset is widely recognized as a benchmark for nodule detection research. It has been extensively used for training deep learning models and comparing the performance of different nodule detection algorithms. Malignancy markers were initially absent from the LUNA16 dataset. We used the metadata CSV file with the LIDC-IDRI dataset to update the radiologists' malignancy markings corresponding to patient IDs. Nodules are marked on a scale of 1 to 5 in the LIDC-IDRI dataset, with one denoting benign and 5 denoting the highest level of malignancy. According to the malignancy score, the annotated nodule with a score less than three is benign, a score equal to three is uncertain, and a score greater than three is malignant.

3.2. Data Prepossessing

Lung CT scans typically display the entire chest cavity; however, pulmonary nodules are only visible in the left and right lobes. Occasionally, spherical tissues resembling nodules near the lobes may hinder accurate identification. To address this challenge, the raw CT data must be pre-processed, and the lung parenchyma needs to be extracted. This approach reduces the detection area and improves the accuracy of subsequent diagnoses.

The Hounsfield Unit (HU) is commonly used to represent CT data and is standardized. It provides a numerical value that indicates the radiodensity of tissues. It can vary across different tissues, leading to discrepancies when comparing regions of interest. This variation is primarily due to the composition and density of the tissues. By adjusting the HU value range, it is possible to control the detecting area and focus on the regions that are most relevant to the

analysis, improving the accuracy of downstream tasks such as segmentation and detection.

The stages involved in data preparation are as follows:

- **Data normalization :** The HU value range for lung parenchyma is between [-1200, 600]. Therefore, we normalize the CT images' HU values to fall within this range [24]. This ensures that all images are consistently represented, regardless of variations in acquisition protocols or scanners.
- **Mapping:** The HU value range is mapped to [0, 1] using Min-Max normalization. This transformation makes the data suitable for machine learning models by scaling it to a standard range, facilitating better model convergence during training.
- **Binarization of Mask:** The provided ground truth mask contains several labels, with 1 representing the background and 3 or 4 representing the left and right lungs. We assign 0 to the background and 1 to both lung regions.
- **Reslicing and Resizing of Image and Mask:** We resize the data to $256 \times 256 \times 256$ and scale it to 1 mm in the x, y, and z dimensions.
- **Labeling Nodules:** We average the malignancy labels of the nodules and classify them as follows: if the mean malignancy level is less than three, the nodule is labelled as benign; if it is greater than three, the nodule is labelled as malignant; and if the mean malignancy level is equal to three, it is labelled as ambiguous.

To prepare data for YOLO-V5, the following steps are taken:

- **Crop foreground:** We crop the space around the segmented lung parenchyma based on the largest foreground region.
- **Generate bounding box:** We use the spherical mask to generate a bounding box for each slice based on the provided diameter and center from the annotation file. The YOLOv5 label format includes the class ID, x-center, y-center, width, and height, with normalized coordinates.

Table 2

Details of Hyperparameters Used for the Models

| Lung Segmentation Task | | Lung Nodule Detection Task | | Lung Nodule Malignancy Classification Task | |
|------------------------|-----------|------------------------------|---------------------|--|---------------------------|
| Hyper-parameters | Values | Hyper-parameters | Values | Hyper-parameters | Values |
| Training data | 800 | Training data | 6045 | Training data | 1577 |
| Test data | 88 | Test data | 756 | Test data | 394 |
| Batch size | 4 | Batch size | 64 | Batch size | 256 |
| Learning rate | 0.0001 | Learning rate | 0.01 | Learning rate | 0.0001 |
| Epoch | 60 | Epoch | 600 | Epoch | 60 |
| Optimizer | Adam | Optimizer | Adam | Optimizer | Adam |
| Loss function | Dice loss | Bounding box regression loss | | Loss function | Categorical-cross entropy |
| | | Loss function | Objectness loss | Patch Size | 8 |
| | | | Classification loss | | |

To train the classification network, a 64×64 slice is cropped from the spherical mask volume according to the diameter and center of the annotation file.

4. Deep learning architectures

4.1. Segmentation Network

Lung CT scans typically display the entire chest cavity of the patient, offering a comprehensive view of the thoracic region. These scans are vital for diagnosing a range of pulmonary conditions. However, they often present challenges in interpretation due to the presence of various structures within the chest, including several spherical tissues adjacent to the lobes. These structures can appear similar to nodules, complicating the analysis and detection process. These misclassifications can lead to false positives or missed diagnoses, making accurate detection of actual nodules difficult. Therefore, it is essential to preprocess the raw CT data to enhance the accuracy of the analysis. This preprocessing involves delineating the lung parenchyma and removing surrounding tissues that may obscure the actual nodules. By isolating the lung parenchyma from other structures, we reduce the area the model needs to process, allowing for more accurate segmentation and detection of nodules.

Additionally, different types of nodules can be present in the lung, some of which are located very close to the lung surface, as shown in Fig. 2. Therefore, maintaining a reliable and precise segmentation network is crucial. This is why we have chosen to employ 3D methods in our approach, as they have demonstrated significantly better performance in lung segmentation tasks than traditional 2D methods. By utilizing 3D models, we are able to capture spatial relationships within the lung tissue more effectively, allowing the model to consider the whole 3D structure of the lungs and improve its accuracy in segmenting the nodule areas.

4.1.1. Baseline Model-3D Unet

Comparable to the standard U-Net [25], our 3D U-Net model consists of an analysis and synthesis path with four resolution stages, with the number of filters being 24, 48, 96, and 192, respectively. Each layer in the analysis path

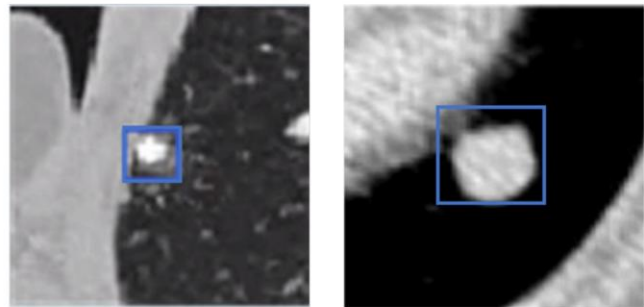


Figure 2: Some instances of nodules very near the lung surface.

contains two $3 \times 3 \times 3$ convolutions, followed by a rectified linear unit (ReLU) activation function and a $2 \times 2 \times 2$ max pooling operation with two strides in each dimension. In the synthesis path, each layer comprises a $2 \times 2 \times 2$ up-convolution with two strides in each dimension, followed by two $3 \times 3 \times 3$ convolutions, each followed by a ReLU activation function.

Shortcut connections from layers of the exact resolution in the analysis path are used to provide the synthesis path with the necessary high-resolution features. In the final layer, a $1 \times 1 \times 1$ convolution reduces the output channels to the number of labels, in this case, 3. The input to the network is a $256 \times 256 \times 256$ voxel image tile, and the output from the last layer is $256 \times 256 \times 1$ voxels in the x, y, and z directions, respectively.

4.1.2. Proposed Model (3D Res-Unet)

The most crucial component of a deep residual network is the residual block, which consists of convolutional layers with identity mapping, as shown in Fig. 3. The residual block is designed to mitigate the vanishing gradient problem and may also enhance information transmission between layers. In this study, four subunits (four convolutional layers within the residual block) were used.

YOLOv5 is a state-of-the-art deep learning model for object detection that utilizes a single neural network to predict object bounding boxes and class probabilities in an input image. This model improves upon its predecessors,

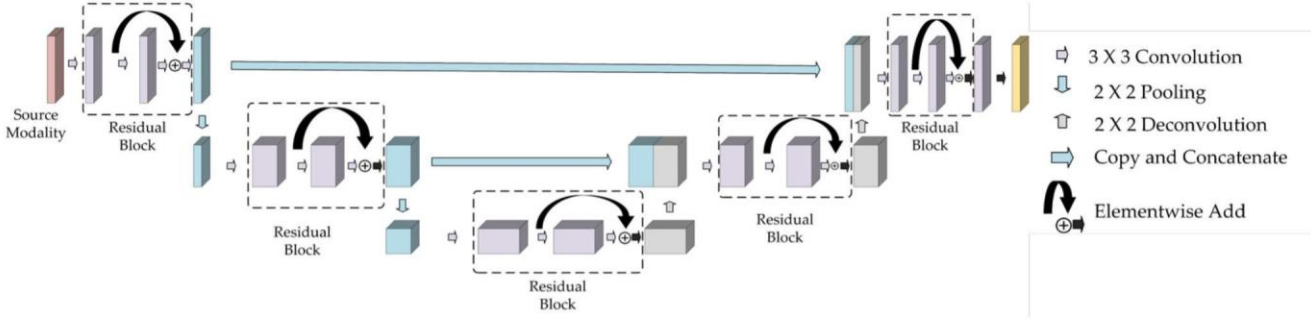


Figure 3: Overview of the proposed 3D Res-UNet architecture

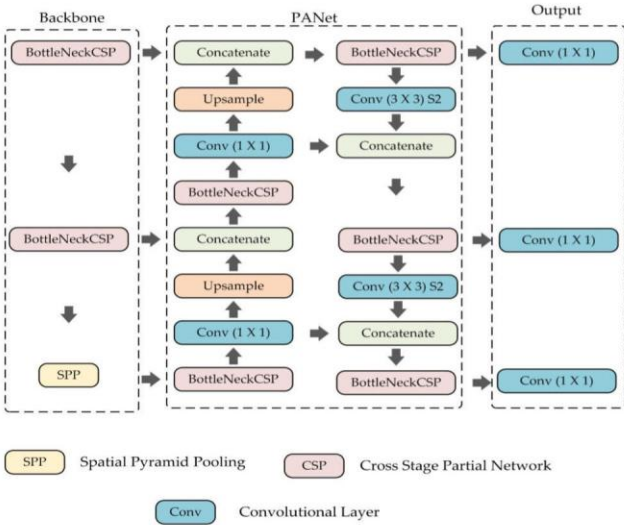


Figure 4: The main components of the YOLOv5 model include the CSPDarknet backbone, the PANet neck, and the YOLO Layer head. In the CSPDarknet, features are extracted from the input data. These extracted features are then combined in the PANet. Finally, the YOLO Layer generates the object detection results, which include the class, score, location, and size of the detected objects.

YOLOv4 and YOLOv3, by incorporating several new techniques to achieve higher accuracy and efficiency. YOLOv5 features a CSPNet (Cross-Stage Partial Network) backbone, an efficient variant of the Darknet backbone used in previous YOLO versions. The CSPNet backbone extracts features from the input image, which are then processed through multiple layers of spatial pyramid pooling (SPP) and path aggregation network (PAN) modules, enhancing the model's ability to capture features at different scales, as shown in Fig. 4.

The YOLOv5 model utilizes anchor boxes to predict object bounding boxes and incorporates a novel loss function called the Generalized Intersection over Union (GIoU) loss for training. The GIoU loss enhances the traditional Intersection over Union (IoU) loss, providing a better measure of the similarity between predicted and ground truth bounding boxes. Additionally, YOLOv5 employs a self-ensemble technique, where multiple versions of the same model make

predictions on the same input image. The predictions from these models are then combined to generate a final prediction, which has been shown to improve accuracy [26].

YOLOv5 is available in several variants, from YOLOv5s (small) to YOLOv5x (extra large). The larger models have more parameters and can achieve higher accuracy but are more computationally expensive to train and run. In this study, we use the small version of YOLOv5 due to computational constraints.

4.2. Classification Network

The Vision Transformer (ViT) is a deep learning architecture for computer vision tasks, introduced by Google researchers in 2020 [27]. Unlike traditional CNNs, ViT utilizes self-attention mechanisms from the transformer architecture to capture global context from images, enabling the model to focus on important features across the entire image rather than local regions. This self-attention mechanism allows ViT to model long-range dependencies, which is especially useful for large, complex images.

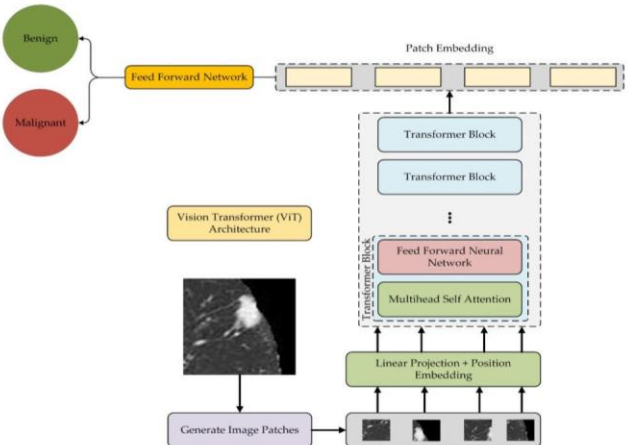


Figure 5: Overview of the proposed vision transformer architecture.

In our proposed ViT network, the input nodule patches are first divided into eight smaller patches. These patches are then subjected to a series of linear transformations, converting them into a sequence of tokens. The tokens are passed through 8 successive transformer encoders, where multi-head self-attention with a projection dimension of 64

and feed-forward layers with 64 and 128 hidden nodes are applied to extract image features. These encoder layers are designed to learn complex relationships between patches, enhancing the model's ability to capture detailed contextual information. Finally, a feed-forward network with sequential hidden states of 2048 and 1024 helps refine the learned features, assisting the final classification layer in predicting the output label. This approach facilitates the model's ability to generalize well, offering accurate predictions across various imaging conditions.

5. Experimental Evaluation

5.1. Experimental Setup

The deep learning architectures are implemented using PyTorch, TensorFlow, and Keras, with all models trained and tested on an Intel® Xeon® CPU and an NVIDIA GTX 2080 Ti GPU. The models were trained on 4 RTX A4500 GPUs, providing a total of 80 GB of GPU memory, with 24 GB of VRAM per GPU. The system also includes an Intel Core i9-10920X CPU with 12 cores, a clock speed of 3.50 GHz, and 256 GB of RAM.

Details regarding the size of training and testing samples for each task, along with all hyperparameters used for training, are provided in Table 2. During training, 10% of the training data was reserved for validation. Furthermore, a mini-batch balancing strategy was employed for classification model training to ensure each batch contained an equal number of samples from each class.

5.2. Evaluation Metrics for Lung Segmentation

The Dice score is a widely used metric for evaluating the performance of lung segmentation algorithms, as it measures the pixel-wise agreement between the predicted lung segmentation and the corresponding ground truth. The Dice score is calculated as follows:

$$\text{Dice Score} = \frac{2 \times |X \cap Y|}{|X| + |Y|} \quad (1)$$

In this formula, X and Y represent two sets, and $|X|$ and $|Y|$ represent their respective cardinalities (i.e., the number of elements in each set). The symbol \cap represents the intersection of the two sets (i.e., the set of elements that are common to both X and Y), and $|X \cap Y|$ represents the cardinality of their intersection. The dice score is a measure of similarity between two sets, with a value ranging from 0 (no similarity) to 1 (perfect similarity).

5.3. Evaluation Metrics for Lung Nodule Detection

To evaluate the performance of the YOLOv5 nodule detection network, two metrics, mAP@50 and mAP@50:95, have been utilized. mAP@50 refers to the mean average precision at a detection threshold of 50% for the official PASCAL VOC (Visual Object Classes) dataset. It is calculated as follows:

$$mAP@50 = \frac{1}{N_{classes}} \sum_{i=1}^{N_{classes}} AP_{50}^i \quad (2)$$

where $N_{classes}$ is the number of object classes, and AP_{50}^i is the average precision for class i at a detection threshold of 50%.

mAP@50:95 is the mean average precision averaged over all recall values between 50% and 95% for the official COCO (Common Objects in Context) dataset. It is calculated as follows:

$$mAP@50 : 95 = \frac{1}{N_{classes}} \sum_{i=1}^{N_{classes}} \int_{0.5}^{0.95} AP(r)dr \quad (3)$$

where $N_{classes}$ is the number of object classes, $AP(r)$ is the average precision at recall level r , and the integral is taken over all recall levels from 50% to 95%.

5.4. Evaluation Metrics for Cancer Classification

The cancer classification LC-ViT framework is evaluated quantitatively using well-known and important performance evaluation metrics such as Accuracy, Precision, Recall, and F1-score. The formulas for these metrics are as follows:

Accuracy(Acc.) measures the proportion of correctly classified samples and is calculated as follows:

$$Acc. = \frac{TP + TN}{TP + FP + TN + FN} \quad (4)$$

Precision measures the proportion of positive samples that are correctly identified and is calculated as follows:

$$Precision = \frac{TP}{TP + FP} \quad (5)$$

Recall measures the proportion of positive samples that are correctly identified out of all the positive samples and is calculated as:

$$Recall = \frac{TP}{TP + FN} \quad (6)$$

F1-score combines both precision and recall into a single metric and is calculated as the harmonic mean of precision and recall:

$$F1\ score = \frac{2 * TP}{2 * TP + FP + FN} \quad (7)$$

Where TP, TN, FP, and FN represent the number of true positives, true negatives, false positives, and false negatives, respectively.

6. Experimental results

6.1. Segmentation Results

We compared the results of our lung segmentation to the expert-provided ground truth lung masks to evaluate the

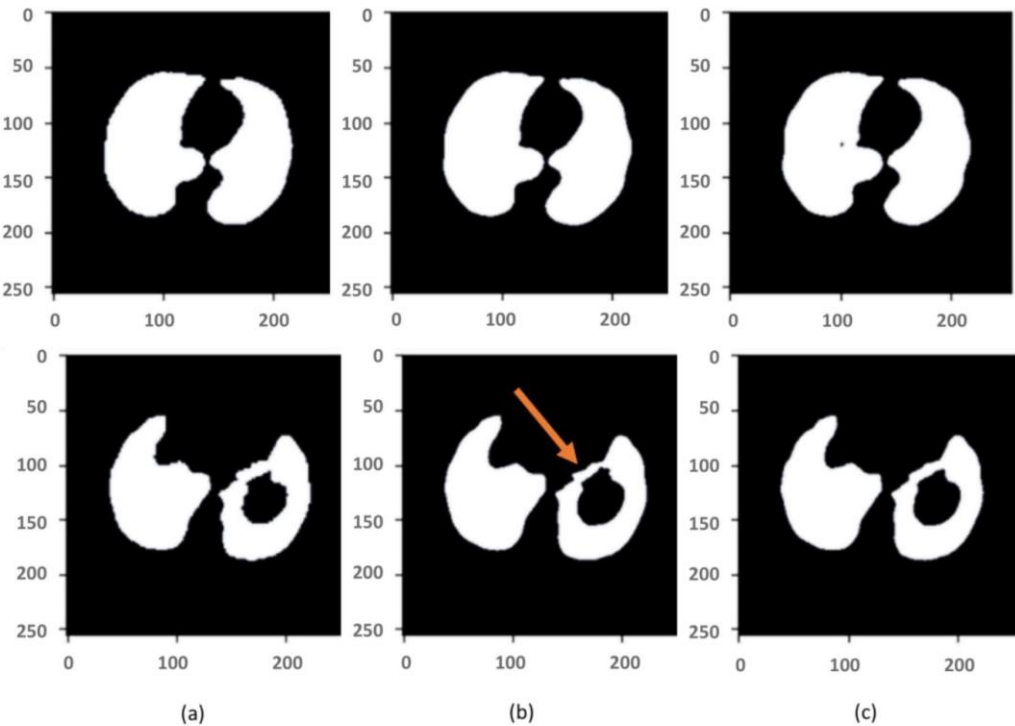


Figure 6: The visual results of lung segmentation for the 3D U-Net and 3D Res-U-Net architectures are shown in the following columns: (a) represents the ground truth, (b) represents the 3D U-Net prediction, and (c) represents the 3D Res-U-Net prediction

effectiveness of the proposed segmentation method. This comparison was necessary to assess how well the model performs in real-world applications, where accuracy and precision are critical. To quantify the comparison, we employed two distinct metrics: Dice score (DSC) and F1-score. To further examine the impact of residual connections on performance, we evaluated the performance of two models, 3D-U-Net and 3D-Res-U-Net, a modified version of 3D-U-Net that incorporates residual connections to improve information flow and gradient propagation.

Table 3 presents the overall performance of these different architectures. Using the LUNA dataset, we achieved average DSC and F1 scores of 97.54 for both the 3D-U-Net and 3D-Res-U-Net models, indicating that our model performed at a high level of accuracy. The 3D-Res-U-Net model highlights the proposed method's ability to generalize well to unseen samples, showing its robustness in segmenting lung structures across a range of input images.

Additionally, the 3D-Res-U-Net outperformed all previous state-of-the-art lung segmentation networks. To ensure that neither overfitting nor underfitting occurred, we also analyzed the learning curve of the proposed approach for lung CT segmentation in terms of dice loss.

We also evaluated the visual outcomes of the proposed method, and Figure 6 shows that there was minimal to no error in generating the lung segmentation mask from the input lung CT images. The segmentation process accurately delineated the lung boundaries, capturing even the subtle details in the lung parenchyma. The 3D-Res-U-Net effectively

Table 3

Comparison of the Proposed Framework with Existing Lung Segmentation Methods

| Author | Network | Dice Score(%) | F1-Score (%) |
|--------------------|--------------|---------------|--------------|
| Kendall et al. [8] | SegNet | 96.52 | 95.75 |
| Alom et al. [9] | R2U-Net | 98.80 | 98.79 |
| Lijing et al. [13] | U-Net | 88.17 | - |
| Jalali et al. [11] | Res-BCDU-Net | 97.31 | 98.05 |
| Our proposed | 3D U-Net | 97.97 | 97.94 |
| | 3D Res-U-Net | 98.82 | 98.73 |

handled the most challenging regions of the lung due to its superior performance, particularly in areas with complex structures. In contrast, the 3D-U-Net struggled to reproduce the complex curvatures of the lung boundaries, as indicated by the red arrow in Fig. 6. This further emphasizes the advantage of the residual connections in the 3D-Res-U-Net, which facilitate more accurate feature learning and improve segmentation results in difficult-to-detect areas.

6.2. Nodule Detection Results

We evaluated YOLOv5(s) alongside other common nodule detection strategies from recent publications to assess its efficacy in single-stage lung nodule detection. This comparison is crucial for determining how well our proposed method performs relative to other well-established models. Table 4 presents the results of this comparison between our model, YOLOv5, YOLOv5s, and Mask R-CNN. When comparing

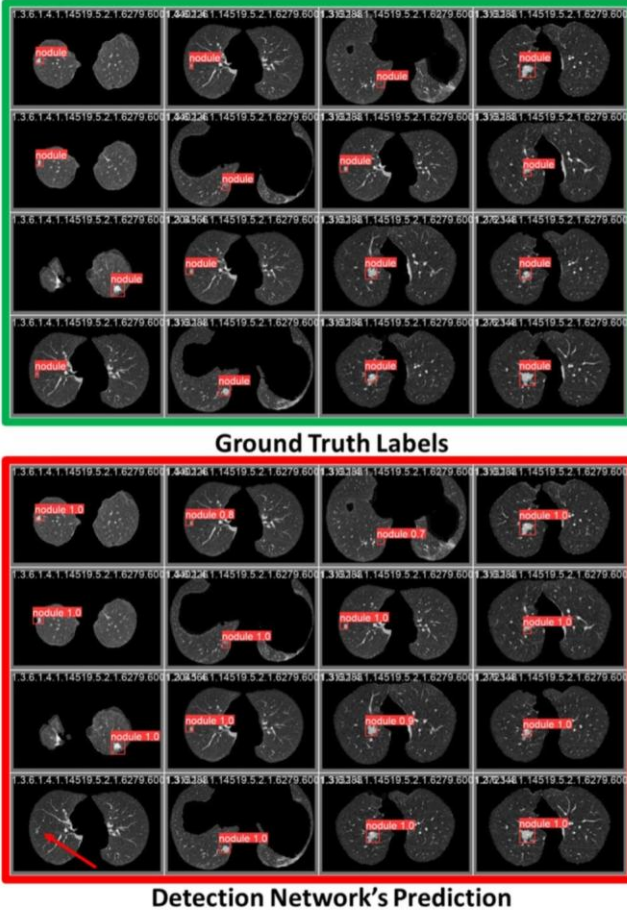


Figure 7: Detection results of nodules on the LUNA16 dataset using YOLOv5(s)

YOLOv5s to the single-stage SSD and the two-stage Mask R-CNN, it can be concluded that YOLOv5s is a more compact and efficient network model. Despite the reduced size, YOLOv5s achieves competitive performance while requiring fewer computational resources. The YOLOv5 model we used consistently performed well compared to other state-of-the-art architectures, demonstrating its robustness in nodule detection. However, STBi-YOLO demonstrated significantly better performance across all models, highlighting its potential for more accurate detection. We also observed that the preprocessing techniques and training data preparation process were not well detailed in [17], which may be a factor influencing the performance discrepancy between our model and others.

We also examined the visual outcomes of the proposed method, and Fig. 7 shows that there was minimal to no error in detecting the lung nodule from the segmented lung CT images. YOLOv5 effectively handled the most challenging nodules, though smaller or less-represented classes were occasionally missed by the detection algorithm, as indicated by the red arrow in Fig. 7. Therefore, YOLOv5 demonstrated its ability to work well on complex cases, including those with irregular shapes and sizes.

Table 4

Comparison of the Proposed Framework with Existing Nodule Detection Methods

| Author | Network | mAP@50 | mAP@50:95 |
|------------------|-----------------|--------|-----------|
| Cai et al. [14] | Mask R-CNN | 0.88 | 0.571 |
| Shao et al. [15] | Yolo v5 refined | 0.75 | - |
| Zhou et al.[16] | Yolo v5(s) | 0.75 | - |
| Liu et al. [17] | STBi-YOLO | 0.95 | - |
| Our Proposed | YOLOv5(s) | 0.76 | 0.62 |

6.3. Cancer Classification Results

We evaluated our proposed Vision Transformer (ViT) algorithm on the LUNA16 dataset and collected diagnostic information from the LIDC-IDRI lung nodule dataset [28], which serves as a primary source of the LUNA16 dataset. This combination of datasets allows us to assess the model's generalizability and robustness across different lung CT images. The LIDC-IDRI dataset provides richly annotated nodules, including malignancy ratings, which enhances the reliability of the evaluation process. Examples of binary-class nodules from the dataset are shown in Fig.8, and Table 5 compares the performance metrics of our proposed model with those of several state-of-the-art (SOTA) methods.

It is important to note that all the studies referenced utilized the LIDC-IDRI database, making it a widely recognized benchmark in lung nodule detection. As shown in the table, our ViT model demonstrates promising performance, outperforming many existing methods. For instance, Wu et al. used STLF-VA classifiers and reported accuracies of 92.36%. In comparison, our model achieved an accuracy of 93.57% and a precision of 90.95%, which represents an improvement of 1.21% in accuracy and 0.02% in precision over the previous top-performing method [22]. This improvement highlights the effectiveness of our ViT architecture in achieving high performance on a complex and challenging task like lung nodule detection.

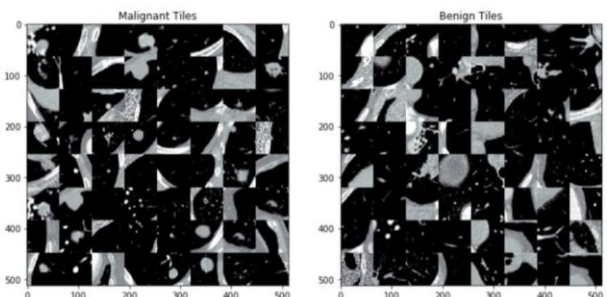


Figure 8: Representation of some malignant and benign nodules

7. Limitations & Future works

Although the proposed framework demonstrated promising results, it requires significant computational resources,

Table 5

Comparison of the Proposed Framework with Existing Nodule's Malignancy Classification Methods

| Author | Network | Acc. (%) | Recall(%) | Precision(%) |
|-------------------|---------|----------|-----------|--------------|
| Filho et al. [19] | CNN | 92.03 | 93.47 | 90.70 |
| Xie et al.[20] | DCNN | 89.93 | 92.02 | 84.19 |
| Huang et al. [21] | SSTL-DA | 91.07 | 91.22 | 90.93 |
| Wu et al. [22] | STLF-VA | 92.36 | 93.08 | 90.93 |
| Our Proposed | ViT | 93.57 | 93.10 | 90.95 |

including powerful GPUs and large amounts of memory. This could limit its practicality in low-resource settings. Additionally, the system has not yet been validated in clinical settings, and further studies are needed to assess its effectiveness in assisting clinicians with primary decisions for lung cancer diagnosis [29, 30].

In the future, we plan to test the framework on larger and more diverse datasets, including in-house datasets, to ensure its broad applicability. Additionally, we aim to integrate this framework into clinical decision support systems to assist radiologists in making accurate diagnoses and treatment plans. However, since deep neural networks are often considered black boxes, we also plan to use gradient-weighted class activation mapping (GradCAM) to enhance the model's interpretability while preserving its complexity [31].

8. Conclusions

In this study, we propose an end-to-end automatic deep neural framework for classifying benign and malignant lung nodules, enabling the detection of lung cancer from CT scans. The ability to detect and classify lung nodules accurately is crucial for early-stage diagnosis, which significantly improves patient outcomes. Our framework integrates three robust architectures: 3D-Res-U-Net, YOLOv5, and ViT, each contributing to different stages of the process. The 3D-Res-U-Net is responsible for precise lung segmentation, YOLOv5 detects the nodules, and ViT is utilized to classify the pathological condition of the nodules. The experimental results demonstrate that the proposed framework reliably segments the lungs, detects nodules, and classifies their pathological condition accurately. These results indicate that our model performs well in handling real-world, complex data. Notably, our ViT architecture achieved an overall accuracy of 93.57%, surpassing other state-of-the-art architectures' performance in lung nodule classification. This improvement highlights the effectiveness of the Vision Transformer (ViT) in capturing global context and fine details from CT images. We believe that our system has the potential to be a valuable tool in clinical decision support, offering a robust, automated solution for lung cancer classification. Furthermore, it can significantly aid primary decision-making, particularly in resource-limited regions where access to expert radiologists and advanced diagnostic tools may be scarce. By reducing the need for manual

intervention and providing timely and accurate results, this system can help bridge the gap in healthcare accessibility.

9. Compliance with Ethical Standards

Author contributions All the works performed by Samiul Based Shuvo and Tasnia Binte Mamun.

Funding None.

Conflict of interest Author certifies that he has no affiliations with or involvement in any organization or entity with any financial interest or non-financial interest in the subject matter or materials discussed in this manuscript.

Ethical approval This article does not contain any studies on human participants or animals performed by the author.

Research involving human participants and/or animals
This article does not contain any studies with human participants or animals performed by the author.

Informed consent This article does not contain any studies on human participants performed by the author.

References

- [1] Freddie Bray, Mathieu Laversanne, Hyuna Sung, Jacques Ferlay, Rebecca L Siegel, Isabelle Soerjomataram, and Ahmedin Jemal. Global cancer statistics 2022: Globocan estimates of incidence and mortality worldwide for 36 cancers in 185 countries. *CA: a cancer journal for clinicians*, 74(3):229–263, 2024.
- [2] Ting-Yuan David Cheng, Susanna M Cramb, Peter D Baade, Danny R Youlden, Chukwumere Nwogu, and Mary E Reid. The international epidemiology of lung cancer: latest trends, disparities, and tumor characteristics. *Journal of Thoracic Oncology*, 11(10):1653–1671, 2016.
- [3] Mahul B Amin. American joint committee on cancer, american cancer society, 2017.
- [4] Huanze Chen, Wangping Xiong, Jia Wu, Qinghe Zhuang, and Genghua Yu. Decision-making model based on ensemble method in auxiliary medical system for non-small cell lung cancer. *IEEE Access*, 8:171903–171911, 2020.
- [5] Jia Wu, Yanlin Tan, Zhigang Chen, and Ming Zhao. Decision based on big data research for non-small cell lung cancer in medical artificial system in developing country. *Computer Methods and Programs in Biomedicine*, 159:87–101, 2018.
- [6] Abhinav Shrivastava, Abhinav Gupta, and Ross Girshick. Training region-based object detectors with online hard example mining. In *Proceedings of the IEEE conference on computer vision and pattern recognition*, pages 761–769, 2016.
- [7] Arnaud Arindra Adiyoso Setio, Alberto Traverso, Thomas De Bel, Moira SN Berens, Cas Van Den Bogaard, Piergiorgio Cerello, Hao Chen, Qi Dou, Maria Evelina Fantacci, Bram Geurts, et al. Validation, comparison, and combination of algorithms for automatic detection of pulmonary nodules in computed tomography images: the luna16 challenge. *Medical image analysis*, 42:1–13, 2017.
- [8] Vijay Badrinarayanan, Alex Kendall, and Roberto Cipolla. Segnet: A deep convolutional encoder-decoder architecture for image segmentation. *IEEE transactions on pattern analysis and machine intelligence*, 39(12):2481–2495, 2017.

[9] Md Zahangir Alom, Chris Yakopcic, Mahmudul Hasan, Tarek M Taha, and Vijayan K Asari. Recurrent residual u-net for medical image segmentation. *Journal of Medical Imaging*, 6(1):014006–014006, 2019.

[10] Anita Khanna, Narendra D Londhe, S Gupta, and Ashish Semwal. A deep residual u-net convolutional neural network for automated lung segmentation in computed tomography images. *Biocybernetics and Biomedical Engineering*, 40(3):1314–1327, 2020.

[11] Yeganeh Jalali, Mansoor Fateh, Mohsen Rezvani, Vahid Abolghasemi, and Mohammad Hossein Anisi. Resbcdu-net: a deep learning framework for lung ct image segmentation. *Sensors*, 21(1):268, 2021.

[12] Seenia Francis, PB Jayaraj, PN Pournami, Manu Thomas, Ajay Thoomkuzhy Jose, Allen John Binu, and Niyas Puzhakkal. Thoraxnet: a 3d u-net based two-stage framework for oar segmentation on thoracic ct images. *Physical and Engineering Sciences in Medicine*, 45(1):189–203, 2022.

[13] Lijing Sun, Mengyi Zhang, Yu Lu, Wenjun Zhu, Yang Yi, and Fei Yan. Nodule-clip: Lung nodule classification based on multi-modal contrastive learning. *Computers in Biology and Medicine*, 175:108505, 2024.

[14] Linqin Cai, Tao Long, Yuhua Dai, and Yuting Huang. Mask r-cnn-based detection and segmentation for pulmonary nodule 3d visualization diagnosis. *Ieee Access*, 8:44400–44409, 2020.

[15] Zisen Shao, Guangze Wang, and Chengwei Zhou. Imageological examination of pulmonary nodule detection. In *2021 2nd International Conference on Big Data & Artificial Intelligence & Software Engineering (ICBASE)*, pages 383–386. IEEE, 2021.

[16] Zhixun Zhou, Fangfang Gou, Yanlin Tan, and Jia Wu. A cascaded multi-stage framework for automatic detection and segmentation of pulmonary nodules in developing countries. *IEEE Journal of Biomedical and Health Informatics*, 26(11):5619–5630, 2022.

[17] Kehong Liu. Stbi-yolo: A real-time object detection method for lung nodule recognition. *IEEE Access*, 10:75385–75394, 2022.

[18] Zichao Liu, Lili Wei, and Tingqiang Song. Optimized yolov11 model for lung nodule detection. *Biomedical Signal Processing and Control*, 107:107830, 2025.

[19] Antonio Oseas de Carvalho Filho, Aristofanes Corrêa Silva, Anselmo Cardoso de Paiva, Rodolfo Acatauassú Nunes, and Marcelo Gattass. Classification of patterns of benignity and malignancy based on ct using topology-based phylogenetic diversity index and convolutional neural network. *Pattern Recognition*, 81:200–212, 2018.

[20] Yutong Xie, Jianpeng Zhang, Yong Xia, Michael Fulham, and Yanning Zhang. Fusing texture, shape and deep model-learned information at decision level for automated classification of lung nodules on chest ct. *Information Fusion*, 42:102–110, 2018.

[21] Hong Huang, Ruoyu Wu, Yuan Li, and Chao Peng. Self-supervised transfer learning based on domain adaptation for benign-malignant lung nodule classification on thoracic ct. *IEEE Journal of Biomedical and Health Informatics*, 26(8):3860–3871, 2022.

[22] Ruoyu Wu, Changyu Liang, Yuan Li, Xu Shi, Jiuquan Zhang, and Hong Huang. Self-supervised transfer learning framework driven by visual attention for benign–malignant lung nodule classification on chest ct. *Expert Systems with Applications*, 215:119339, 2023.

[23] Samuel G Armato III, Geoffrey McLennan, Luc Bidaut, Michael F McNitt-Gray, Charles R Meyer, Anthony P Reeves, Binsheng Zhao, Denise R Aberle, Claudia I Henschke, Eric A Hoffman, et al. The lung image database consortium (lidc) and image database resource initiative (idri): a completed reference database of lung nodules on ct scans. *Medical physics*, 38(2):915–931, 2011.

[24] Weijun Tan and Hongwei Guo. Data augmentation and cnn classification for automatic covid-19 diagnosis from ct-scan images on small dataset. In *2021 20th IEEE International Conference on Machine Learning and Applications (ICMLA)*, pages 1455–1460. IEEE, 2021.

[25] Olaf Ronneberger, Philipp Fischer, and Thomas Brox. U-net: Convolutional networks for biomedical image segmentation. In *Medical Image Computing and Computer-Assisted Intervention–MICCAI 2015: 18th International Conference, Munich, Germany, October 5–9, 2015, Proceedings, Part III* 18, pages 234–241. Springer, 2015.

[26] Glenn Jocher, Ayush Chaurasia, Alex Stoken, Jirka Borovec, NanoCode012, Yonghye Kwon, Kalen Michael, TaoXie, Jiacong Fang, imyhxy, Lorna, Zeng Yifu, Colin Wong, Abhiram V, Diego Montes, Zhiqiang Wang, Cristi Fati, Jebastin Nadar, Laughing, and Mrinal Jain. ultralytics/yolov5: v7.0 - YOLOv5 SOTA Realtime Instance Segmentation (v7.0), 2022.

[27] Alexey Dosovitskiy, Lucas Beyer, Alexander Kolesnikov, Dirk Weissenborn, Xiaohua Zhai, Thomas Unterthiner, Mostafa Dehghani, Matthias Minderer, Georg Heigold, Sylvain Gelly, et al. An image is worth 16x16 words: Transformers for image recognition at scale. *arXiv preprint arXiv:2010.11929*, 2020.

[28] Samuel G Armato III, Geoffrey McLennan, Luc Bidaut, Michael F McNitt-Gray, Charles R Meyer, Anthony P Reeves, Binsheng Zhao, Denise R Aberle, Claudia I Henschke, Eric A Hoffman, et al. The lung image database consortium (lidc) and image database resource initiative (idri): a completed reference database of lung nodules on ct scans. *Medical physics*, 38(2):915–931, 2011.

[29] Jyotibdha Acharya and Arindam Basu. Deep neural network for respiratory sound classification in wearable devices enabled by patient specific model tuning. *IEEE transactions on biomedical circuits and systems*, 14(3):535–544, 2020.

[30] Seyed Yahya Nikouei, Yu Chen, Sejun Song, Ronghua Xu, Baek-Young Choi, and Timothy R Faughnan. Real-time human detection as an edge service enabled by a lightweight cnn. In *2018 IEEE International Conference on Edge Computing (EDGE)*, pages 125–129. IEEE, 2018.

[31] Hui Wen Loh, Chui Ping Ooi, Silvia Seoni, Prabal Datta Barua, Filippo Molinari, and U Rajendra Acharya. Application of explainable artificial intelligence for healthcare: A systematic review of the last decade. *Computer Methods and Programs in Biomedicine*, 226:107161, 2022.